Bachelor Thesis

SU(2) Lattice Yang-Mills Theory with Open Boundary Conditions

Hannah Müller

20th May 2025

Institut für theoretische Physik
Goethe Universität
Frankfurt am Main

1st Supervisor:
Prof. Dr. Marc Wagner
Institut für theoretische Physik
Goethe Universität
Frankfurt am Main

2nd Supervisor:
Prof. Dr. Owe Philipsen
Institut für theoretische Physik
Goethe Universität
Frankfurt am Main

Selbstständigkeitserklärung

Ich versichere hiermit, dass ich die vorliegende Arbeit selbstständig verfasst und keine anderen als die angegebenen Quellen und Hilfsmittel verwendet habe.
Alle Stellen und Textpassagen, die wörtlich oder sinnentsprechend aus veröffentlichten Quellen oder anderen fremden Texten entnommen sind, sind als solche kenntlich gemacht. Ebenso wurden alle Abbildungen, sofern nicht selbst von mir erstellt, mit entsprechenden Quellennachweisen versehen.
Diese Arbeit wurde noch nicht, auch nicht auszugsweise, für eine andere Studien- oder Prüfungsleistung verwendet.

Ort, Datum

Unterschrift

Abstract

In lattice QCD simulations approaching the continuum limit, configurations often become trapped within specific topological charge sectors, potentially leading to biased results or requiring unaffordable long simulation times. This problem arises particularly with periodic boundary conditions, where transitions between topological sectors are suppressed. To address this, open boundary conditions, in particular Neumann boundary conditions, in the time direction are used, where the derivative of the gauge field $A_\mu(x)$ is set to zero at $t = 0$ and $t = T$. This enables the topological charge to fluctuate more rapidly. However, it introduces boundary effects, which are analyzed in this thesis.
We find that the range in which plaquettes and Wilson loops experience boundary effects is equal for different numbers of lattice points and decreases for smaller lattice spacings. The effects increase as the loops get bigger, even for loops perpendicular to the direction with open boundary conditions. Open boundary conditions are expected to become efficient for lattice spacings smaller than 0.05 fm when topological freezing is found to appear.

Contents

1 Introduction

Quantum chromodynamics (QCD) is a quantum field theory describing the interaction between quarks and gluons. In this context, quarks and gluons are represented by quantum fields. This allows the description of dynamic particle creation and annihilation processes. Quarks carry a color charge that cannot be observed externally. Also, the exchange particles themselves carry a color charge and thus can interact with each other. In QCD one key phenomenon is confinement, which means that quarks and gluons cannot be observed as free particles, but are always colorneutrally bound in hadrons. Another phenomenon is asymptotic freedom, meaning that the coupling decreases at high energies. At low energies the coupling is strong, making perturbation theory unreliable. [1, 2]

To describe particles in QCD and the gauge field dynamics of non-Abelian fields with static quarks, a SU(N) gauge theory, called Yang-Mills theory is applied. Specifically, local SU(3) color invariance is demanded. [2] To simplify the calculations, the SU(2) group is used. The SU(2) group is qualitatively similar to the SU(3) group, as it shows the same mechanisms such as confinement and the topological charge. While the computational complexity is reduced, systematic deviations compared to full QCD are introduced.

In lattice QCD, the space-time gets discretized, while the gauge symmetry is preserved. To approach the continuum limit, very small lattice spacings need to be simulated. For spacings $a \approx 0.01$fm, calculations of physical quantities such as the quark-antiquark potential become particularly interesting.
Often, periodic boundary conditions are implemented which makes the space-time a four dimensional torus. Field configurations, obtained from Monte Carlo simulations, are classified by the so called topological charge which is the sum of instantons on the lattice. When using periodic boundary conditions the topological charge is quantized, which indicates the existance of different topological sectors. The charge can change through tunneling. The tunneling probability is suppressed when the lattice spacing gets smaller. Consequently, the topological charge has extremely long autocorrelation times. When approaching the continuum limit, lattice QCD simulations get trapped in one topological sector, which is called topological freezing. This leads to biased results or unreasonable long simulation times, since the simulation time needs to be several times longer than the autocorrelation time.
The impact of different boundary conditions on the autocorrelation of the topological charge has already been analyzed in detail by Martin Lüscher and Stefan Schaefer [3] as well as by Simon Mages et al. [4].

The problem of topological freezing can be solved by using open boundary conditions in one or more directions. Neumann boundary conditions are applied to the gauge field, while gauge symmetry and the gauge degrees of freedom are preserved. The field space becomes connected in the continuum limit, because the topological charge can flow freely and consequently becomes continuous and changes faster. Although the autocorrelation time is greatly reduced, boundary effects are introduced as a consequence. [3, 4]

This thesis is structured as follows: In section 2 the SU(N) Yang-Mills theory is presented, in the continuum and on the lattice. Plaquettes and Wilson loops which are necessary for computing the static quark-antiquark potential are defined. Periodic and open boundary conditions are discussed in section 3 including their meaning for the topological charge.
The boundary effects resulting from open boundary conditions in time direction are analyzed in section 4.1 for plaquettes and Wilson loops of different sizes. This is compared for loops parallel and perpendicular to time direction for different lattice sizes and lattice spacings. Finally, the effects on the topological charge for periodic boundary conditions with different lattice spacings are considered in section 4.2, to estimate the efficiency of open boundary conditions.

2 SU(2) Yang-Mills theory on the lattice

2.1 Yang-Mills theory

Yang-Mills theory is a quantum field theory based on SU(N) gauge symmetry. The following definitions are taken from reference [2]. In QCD, the gauge group is SU(3), but to simplify the calculations we replace the SU(3) group by the SU(2) symmetry group. The Lagrangian density of SU(N)-gauge theory is invariant under global SU(N) gauge transformations. The local SU(N) gauge symmetry, required by the gauge principle, leads to a modified Lagrangian density with exchange particles carrying a charge themselves.
In QCD local SU(3) color symmetry is demanded. Therefore, the Lagrangian density, shown further below, is modified accordingly by introducing the covariant derivative

$$\partial_\mu \to D_\mu = \partial_\mu - igA_\mu^a T^a \tag{1}$$

with the coupling g, the color-indices a, $T^a = \frac{\lambda^a}{2}$ and the generator of the SU(3) color group, the Gell-Mann-matrices λ^a. The gauge fields $A_\mu^a(x)$ are the gluon fields, for which a dynamic term is added, including the field strength tensor

$$F_{\mu\nu}^a = \partial_\mu A_\nu^a - \partial_\nu A_\mu^a + gf_{abc}A_\mu^b A_\nu^c. \tag{2}$$

f_{abc} are the structure constants. Combining all these elements, the QCD Lagrangian density has the form

$$\mathcal{L}_{\mathrm{QCD}} = \sum_{c=1}^{N_c}\sum_{f=1}^{N_f} \bar{q}_{fc}(i\gamma^\mu D_\mu - m_f)q_{fc} - \frac{1}{4}F_{\mu\nu}^a F^{a\,\mu\nu}. \tag{3}$$

q_{fc} are quark fields with flavor f, color c and mass m_f. $\bar{q}_{fc}$ represents antiquarks, γ^μ are the gamma matrices and $F_{\mu\nu} = F_{\mu\nu}^a T^a$. In SU(2) gauge theory, the Lagrangian density needs to be invariant under local SU(2) transformations. This transformation is given by the 2×2 matrix

$$U = e^{-i\theta^a T^a} \in SU(2), \qquad a = 1, 2, 3 \tag{4}$$

using Pauli matrices as generators:

$$T^a = \frac{\sigma^a}{2}. \tag{5}$$

2.2 Lattice gauge theory

When describing strong interactions, the gauge symmetry needs to be preserved while introducing the discretized space-time lattice. [1] For the four-dimensional lattice $\Lambda = \{n = (n_0, n_1, n_2, n_3) \mid n_\mu = 0, .., N_\mu - 1\}$ with spatial extent L and time extent T the gauge field $A_\mu(x)$ is introduced as oriented link variables $U_\mu(n) \in SU(2)$ connecting the sites n and $n + \hat{\mu}$, at a distance of lattice spacing a. With $\Omega(n) \in SU(2)$ the gauge transformation is given by [5]:

$$U_\mu(n) \to U'_\mu(n) = \Omega(n)U_\mu(n)\Omega^\dagger(n + \hat{\mu}) \tag{6}$$

and one defines

$$U_\mu(n) = e^{iaA_\mu(n)}. \tag{7}$$

The trace of a product of such link variables forming a closed loop is gauge-invariant and thus is a physical observable. Also, loops are needed for the gluon action. A plaquette is the shortest, nontrivial closed loop on the lattice and the plaquette variable is given by [5]

$$P_{\mu\nu}(n) = U_\mu(n)U_\nu(n+\hat{\mu})U_\mu(n+\hat{\nu})^\dagger U_\nu(n)^\dagger. \tag{8}$$

The relation between these plaquettes and the field strength tensor $F_{\mu\nu}$ is provided by:

$$P_{\mu\nu}(n) = e^{ia^2 F_{\mu\nu}(n) + \mathcal{O}(a^3)} \tag{9}$$

Wilson action The mentioned relation of the field strength tensor and the plaquettes allows the discretisation of the action. The QCD action is the sum of the quark and gluon actions, where the gluon action only depends on the gluon field [1]. As a result, the Wilson gauge action can be calculated from the sum of the plaquettes [5]:

$$\begin{aligned} S_G[U] &= \frac{\beta}{N} \sum_{n\in\Lambda} \sum_{\mu<\nu} \mathrm{Re}\,\mathrm{tr}\left[\mathbf{1} - P_{\mu\nu}(n)\right] \\ &= \frac{a^4}{2g^2} \sum_{n\in\Lambda} \sum_{\mu<\nu} \mathrm{tr}\left[F_{\mu\nu}(n)^2\right] + \mathcal{O}(a^2) \\ &\xrightarrow{a\to 0} S_G[A] \end{aligned} \tag{10}$$

$\beta = \frac{2N}{g^2}$ is the inverse lattice coupling and g the coupling.

Eigenvalues and path integrals Expectation values in pure gauge theory can be calculated analogously to quantum mechanics. In QM, path integrals are used to calculate ground state expectation values, where it is integrated over all possible paths weighted with the respective actions. In QCD the expectation values are calculated in the QCD ground state $|\Omega\rangle$ for observables $O[\psi, \overline{\psi}, A]$ composed of quark and gluon fields [1]. Using pure gauge theory on the lattice, the expectation values can be calculated as follows [5]:

$$\begin{aligned} \langle O \rangle &= \frac{1}{Z} \int D[U]\, e^{-S_G[U]} O[U], \\ Z &= \int D[U]\, e^{-S_G[U]}. \end{aligned} \tag{11}$$

Z is the partition function and the integration measure is $\int D[U] = \prod_{n\in\Lambda} \prod_{\mu=1}^{4} \int dU_\mu(n)$. The measure for a single link variable is $dU_\mu(n)$.

2.3 Wilson loops and the static quark-antiquark potential

Wilson loops are observables that can be related to the static quark-antiquark potential $V(r)$. The Wilson loops are defined as the trace of the product of link variables along a closed loop $\mathcal{L}$ ([5], section 3.3):

$$W_{\mathcal{L}}[U] = \mathrm{tr}\left[S(\mathbf{m}, \mathbf{n}, n_t) T(\mathbf{n}, n_t)^\dagger S(\mathbf{m}, \mathbf{n}, 0)^\dagger T(\mathbf{m}, n_t)\right] = \mathrm{tr}\left[\prod_{(k,\mu)\in\mathcal{L}} U_\mu(k)\right]. \tag{12}$$

$S(\mathbf{m}, \mathbf{n}, n_t)$ are the Wilson lines connecting the spatial points $\mathbf{m}, \mathbf{n}$ and $T(\mathbf{n}, n_t)$ are the temporal transporters, that is, a straight line of n_t link variables in time direction, all at the same spatial position $\mathbf{n}$. Wilson loops are gauge-invariant objects. When fixing the gauge, the expectation value remains unchanged, so the temporal gauge, which sets all time links to $\mathbf{1}$, can be applied for simplicity.

$$\begin{aligned}
\langle W_{\mathcal{L}} \rangle &= \langle W_{\mathcal{L}} \rangle_{temp} \\
&= \langle \mathrm{tr}[S(\mathbf{m}, \mathbf{n}, n_t) S(\mathbf{m}, \mathbf{n}, 0)^\dagger] \rangle_{temp} \\
&= \sum_k \langle 0 | S(\mathbf{m}, \mathbf{n})_{ab} | k \rangle \langle k | S(\mathbf{m}, \mathbf{n})^\dagger_{ba} | 0 \rangle e^{-tE_k}
\end{aligned} \tag{13}$$

The sum over all energy eigenvalues $|k\rangle$ with nonvanishing overlap with $S(\mathbf{m}, \mathbf{n})^\dagger |0\rangle$ are states describing the static quark-antiquark pair located at spatial positions $\mathbf{m}, \mathbf{n}$.
The ground state energy E_1 can be extracted by analyzing the long-time behavior ($t \to \infty$) of the Wilson loops. The corresponding potential $V(r)$ of the quark-antiquark pair is obtained from the behaviour of the Wilson loops at large temporal extent n_t: [5]

$$\begin{aligned}
\langle W_{\mathcal{L}} \rangle &\propto e^{-tE_1} \left(\mathbf{1} + \mathcal{O}\left(e^{-t\Delta E} \right) \right) \\
&= e^{-n_t a V(r)} \left(\mathbf{1} + \mathcal{O}\left(e^{-n_t a \Delta E} \right) \right)
\end{aligned} \tag{14}$$

The static potential (eq. (15)) is found to have a linear rising term in the limit of strong coupling g, where σ is the string tension, as well as a Coulomb part with strength B for small coupling. A is a constant shift, dependent on the lattice spacing. [5]

$$V(r) = A + \frac{B}{r} + \sigma r \tag{15}$$

At large separations, the energy keeps rising linearly when pulling the quark-antiquark pair apart. Because of the self-interaction between gluons the field gets squeezed into a narrow flux tube between the quark and antiquark. If the energy is large enough a new pair of light quarks can be created that recombines with the initial pair. This is called "string breaking". [5]

3 Boundary conditions and the topological charge

For lattice calculations, the space-time is discretized as follows: $x_\mu \in \mathbb{R}^4 \to x_\mu = n_\mu a$ with the lattice spacing a and $n_\mu \in \mathbb{Z}^4$. The extent of the lattice in each spatial direction is $L = aN_L$, with N_L the number of lattice sites in each spatial direction and analogously $T = aN_T$ is the extent in time direction with N_T lattice points. The theory is defined on a finite region of space-time. To have an unambiguous physical situation that is mathematically complete, it must be specified what happens at the boundaries of the lattice. That means, it needs to be defined how the field behaves at those edges, e.g. does it vanish, reflect or continue. One criterion to decide which boundary condition is reasonable, is the fluctuation of the topological charge, introduced in section 3.3.

3.1 Periodic boundary conditions

Periodic boundary conditions are commonly used because they simulate infinite space with a finite volume, which conveniently provides translational invariance. Although periodic boundary conditions differ from an infinitely large volume, they have the advantage of avoiding boundary effects, which simplifies simulations and makes them more efficient.
The link variables at the boundaries embody periodicity in each space-time direction according to

$$U_\mu(N_T, n_1, n_2, n_3) = U_\mu(0, n_1, n_2, n_3). \tag{16}$$

If the space-time is periodic in all directions, each direction behaves like a circle. Consequently, the space-time has the shape of a four-dimensional torus. This preserves the discrete translation symmetry ([5], section 4.2) and leads to small finite volume corrections [4]. With these conditions, plaquettes and Wilson loops can be calculated across the boundaries of the lattice and it can be averaged over all possible realizations ([5], section 4.4).

3.2 Open boundary conditions

Open boundary conditions in time direction imply that time extends from 0 to T, while the space directions satisfy periodic boundary conditions and thus result in a three-dimensional torus. A specific form of open boundary conditions are Neumann boundary conditions. These are applied to $A_\mu(x)$ by setting the gauge-field tensor to fixed values:

$$F_{0k}(x)|_{x_0=0} \;=\; F_{0k}(x)|_{x_0=T} \;=\; 0 \quad \text{for all} \quad k = 1, 2, 3. \tag{17}$$

Using these conditions, the gauge symmetry and consequently the gauge degrees of freedom are preserved. [3] Open boundary conditions replace the torus with another topology, which changes the connectivity of the configuration space. However, due to the lack of translational invariance in the direction with open boundaries, boundary effects arise, reducing the space-time volume available for further calculations. [4]

3.3 Topological charge

When calculating observables on the lattice, high precision and a reliable error estimation are needed. One common error comes from the autocorrelation of consecutive configurations generated with a Monte Carlo algorithm. To achieve meaningful results, the simulation time needs to be several times longer than the longest occuring autocorrelation time. Observables related to the topology of the field, such as the topological charge, have one of the longest autocorrelation times and thus provide a good estimation of the efficiency of the simulation. [4]
Gauge field configurations are classified by their topological charge Q and the corresponding topological sectors. The topological charge is the subtraction of the number of instantons with positive and negative charge on the lattice. Instantons are pseudo-particles with a non local field [6] and their amount can change by tunneling between the topological sectors. To have a representable set of configurations, they must differ in their topological sectors.
On the lattice, the sectors are correctly referred to as pseudo topological sectors. The ensembles of configurations with the same topological charge are seperated by a large Euclidean action. A change between these pseudo topological sectors is possible via continuous transformations. Particularly, a transition becomes possible because the action barriers are not infinite and a Monte Carlo step is not a continuous transformation. Hence, transitions are only suppressed which leads to a large autocorrelation time.
When approaching the continuum limit the pseudo topological sectors merge into topological sectors. In the continuum, these sectors are a set of configurations separated by an infinite action. A continuous deformation between sectors becomes impossible.
The topological charge described in the following was computed on the lattice and therefore refers to pseudo topological sectors. These are commonly referred to as topological sectors for simplicity. [3, 6]

There are different definitions of the topological charge which will lead to different results on the lattice due to discretization, but which become the same integer in the continuum. In this thesis the field definition based on the gluonic fields is used (for other definitions see e.g. [6]).
The topological charge is defined by [4]:

$$\begin{aligned} Q &= \int_{\mathcal{M}} d^4x \; q(x), \\ q(x) &= \frac{1}{32\pi^2} \epsilon_{\mu\nu\rho\sigma} \; \mathrm{tr}\left[F_{\mu\nu} F_{\rho\sigma}\right]. \end{aligned} \tag{18}$$

Here $q(x)$ is the topological charge density and $\mathcal{M}$ the manifold.
On the lattice, the integral can be replaced by a sum over all lattice sites

$$Q = \frac{1}{32\pi^2} \sum_n \sum_{\mu,\nu,\rho,\sigma=0}^{3} \epsilon_{\mu\nu\rho\sigma} \hat{F}_{\mu\nu} \hat{F}_{\rho\sigma} + \mathcal{O}(a^2), \tag{19}$$

where $\hat{F}_{\mu\nu} = \mathrm{Im}(P_{\mu\nu}) + \mathcal{O}(a)$, using the plaquette $P_{\mu\nu}$. The resulting $\mathcal{O}(a^2)$ error of the topological charge leads to non-integer values when using finite lattice spacings, because of discretization, while the correct topological charge should be obtained in the continuum limit.
Moreover, instantons have a positive contribution to the topological charge. If the maximum is not on a lattice point, $\sum_n \sum_{\mu,\nu,\rho,\sigma=0}^{3} \epsilon_{\mu\nu\rho\sigma} \hat{F}_{\mu\nu} \hat{F}_{\rho\sigma}$ results in values slightly below one. Analogously, anti-instantons have a contribution of values slightly above minus one. Consequently, the absolute values of the topological charge are in average a bit below the actual number of instantons. [6]

To reduce those $\mathcal{O}(a^2)$ errors, it is efficient to use different, higher loop operators. As an example, the clover improvement can be used, which replaces the plaquette $\hat{P}^{\mu\nu}$ by the operator $\hat{P}_c^{\mu\nu}$ depicted in fig. 1. [6]

$\hat{P}_c^{\mu\nu} =$ 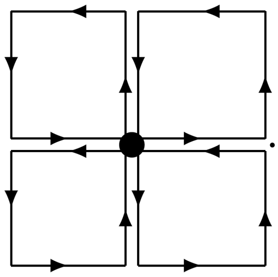 .

Figure 1: Definition of the operator $\hat{P}_c^{\mu\nu}$ for the cloverleaf discretization: four plaquettes arranged in a cloverleaf pattern. [6]

For the density, the cloverleaf discretization is defined as follows [7]:

$$q(x) = \frac{1}{32\pi^2} \sum_{\mu,\nu,\rho,\sigma=0}^{3} \epsilon_{\mu\nu\rho\sigma} \ \mathrm{tr}\left[C_{\mu\nu}^{\mathrm{clov}}(x) C_{\rho\sigma}^{\mathrm{clov}}(x)\right] \tag{20}$$

$$C_{\mu\nu}^{\mathrm{clov}}(x) = \frac{1}{4} \mathrm{Im}\left(P_{\mu\nu}(x) + P_{\nu-\mu}(x) + P_{-\mu-\nu}(x) + P_{-\nu\mu}(x)\right)$$

To achieve integer values, a rescaling as well as further improvements that lead to a suppression of errors below $\mathcal{O}(a^6)$ are required [6], which are not part of this thesis.

Further errors arise from UV-fluctuations, which appear as statistical noise. These would cancel each other out when averaging over independent configurations, but lead to biased results when computing the topological charge for single configurations. The fluctuations appear as peaks in the field, which are seen as instantons. To reduce this effect, 4-dimensional APE-smearing (section C) is applied.

Topological susceptibility The topological charge follows a normal distribution and is related to the topological susceptibility [6]. The average of the distribution is zero thus the variance reduces to

$$\left\langle Q^2 \right\rangle - \left\langle Q \right\rangle^2 = \left\langle Q^2 \right\rangle. \tag{21}$$

and $\left\langle Q^2 \right\rangle$ contains all required information about the distribution. The topological susceptibility is given by

$$\chi = \frac{\left\langle Q^2 \right\rangle}{V}. \tag{22}$$

Here V is the volume of the lattice.
For $SU(2)$ the susceptibility is $\chi^{1/4} = 200(15)\,\mathrm{MeV}$ [8], where $\frac{1}{\mathrm{fm}} = 197.3\,\mathrm{GeV}$.
The topological susceptibility is related to the vacuum energy and provides information contributing to the explanation of the large η'- mass [6].

3.3.1 Topological charge on a lattice with periodic boundary conditions

With periodic boundary conditions, instantons that exit the lattice on one side reenter it on the opposite side. This leads to an integer number of instantons and consequently, an integer topological charge. Also, the total number is constant, since the creation and annihilation of instantons happen in pairs.

As the lattice spacing becomes smaller, the energy barriers of the topological charge sectors become higher, Monte-Carlo steps become smaller and thus transitions between sectors are rarer. The sectors are still connected, but transitions in between are suppressed in the simulations. In the continuum limit the topological sectors would become completely disconnected, as depicted in fig. 2. When approaching the continuum limit, the topological charge cannot flow through the lattice boundaries freely and the simulations can get trapped in one sector. This is called "topological freezing" or "topological slowing down" and is expected for lattice spacings smaller than $a = 0.05\,\mathrm{fm}$ [7]. In this case simulations are biased, especially if the simulation time is still reasonable. The autocorrelation time was found to increase proportionally to the sixth power of the inverse lattice spacing. [3, 4, 6]

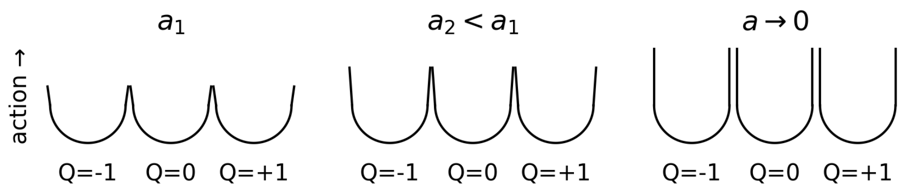

Figure 2: Topological sectors for periodic boundary conditions. When the lattice spacing a decreases, the barriers become higher and tunneling between sectors is suppressed. Approaching the continuum limit the sectors disconnect, which leads to topological freezing.

3.3.2 Topological charge on a lattice with open boundary conditions

Open boundary conditions are one solution to topological freezing. Changing the manifold of the field by using open boundary conditions changes the topology of the space-time as well as of the configurations.
When using open boundary conditions, the number of instantons with positive and negative charge is not well defined. That is because the field space becomes connected in the continuum limit, as the action barrier between the sectors disappears. This implies that the topological charge can flow through the boundaries of space-time freely and is no longer an integer number. Instead, the topological charge becomes continuous and all sectors can be reached during the simulation. This reduces the autocorrelation time of the topological charge drastically. Consequently, the results are less biased by consecutice configurations and observables can be calculated more precisely in a shorter simulation time. [3, 4, 6]

4 Results

A Monte Carlo heatbath algorithm, written in C and provided by Marc Wagner, generates the gauge field configurations. The code has been extended by open boundary conditions and measurements of the topological charge. Additionally, the Jackknife method (section B), as well as an extension to four-dimensional APE-smearing (section C) and a test for gauge invariance (section D) have been implemented.
To generate the configurations, positive and negative staples are calculated at each lattice point and from these, the local action is determined. Plaquettes and Wilson loops are calculated for each configuration. The termalization is shown in section A.
The results are compared for different lattice spacings a further below. This is achieved by using different inverse couplings β. These relations are shown in table 1.

β	a [fm]	$N_T \times N_L^3$
2.4	0.102	$16 \times 16^3, 32 \times 16^3$
2.5	0.073	16×16^3
2.6	0.050	16×16^3

Table 1: With choosing the coupling β the lattice spacing is set. The lattice spacings a in physical units for the used couplings β are chosen between 0.102 fm and 0.05 fm.[9] In this range topological freezing is expected to become noticeable. The lattice sizes are chosen to be equal in lattice units for all spacings, with an additional larger lattice considered only for $\beta = 2.4$.

Open boundary conditions in time direction are implemented by restricting the indices to the valid range. Thus the link variables differ at the boundaries, vanish outside of the lattice and loops are only calculated between the boundaries. Additionally, the spatial plaquettes at the boundaries have weight $\frac{1}{2}$ [3]. Loops are calculated for all positions in time direction separately to visualise the boundary effects.
A distinction is made between loops parallel and perpendicular to time direction as depicted in fig. 3. Perpendicular loops are located entirely at a fixed position in the time direction and maintain a constant distance from the temporal boundary. As a result, all links within one loop are equally affected by the boundary effects. In contrast, loops parallel to the time direction extend across different time positions, they reach closer to or further away from the boundaries. Therefore, the links within one loop experience a different strength of boundary effects.

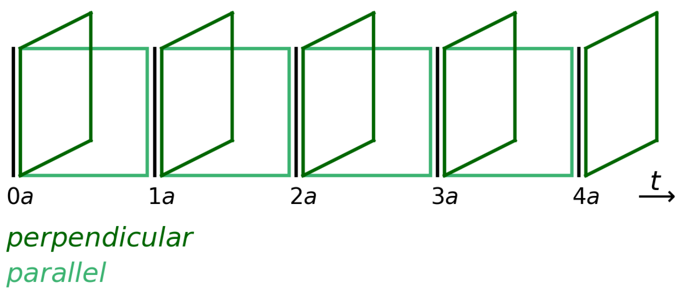

Figure 3: Loops parallel and perpendicular to time direction. Perpendicular loops lie at fixed time positions, parallel loops vary in distance from the boundaries.

4.1 Boundary effects

The figs. 4 to 7 show the values of average loops at different distances from the boundary of the lattice in physical units fm. The results with open boundary conditions are normalized by the average values for periodic boundary conditions, which are represented by the horizontal gray lines. Normalizing is necessary for having comparable results, because a smaller spacing leads to an increase in fluctuation and thus a higher energy density. The plots show half the lattice extension since the results are symmetric.
The average plaquettes and Wilson loops are evaluated after the thermalization phase. The thermalization for periodic and open boundary conditions are compared in section A. The errors are determined using the jackknife method as described in section B.

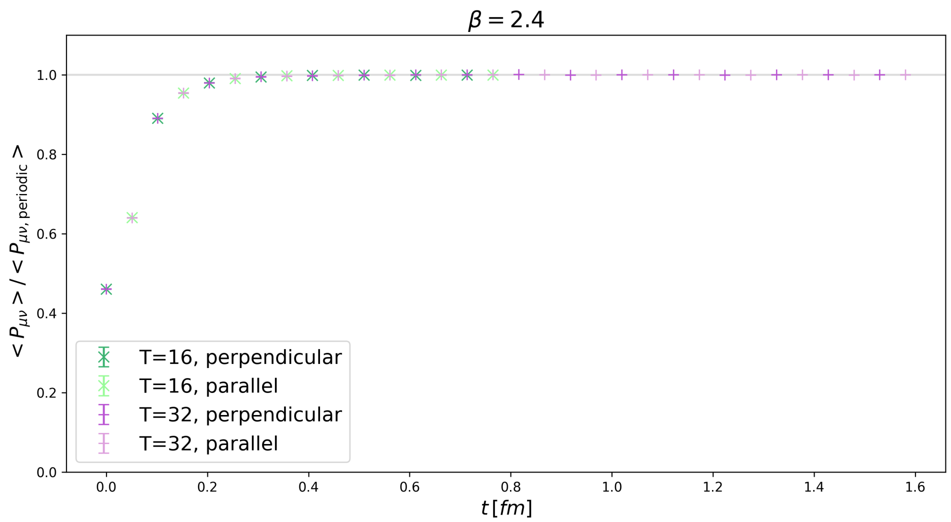

Figure 4: Boundary effects of parallel and perpendicular plaquettes for different lattice sizes $T = 16$ and $T = 32$.

The first interesting result is that for plaquettes only a finite number of lattice points near the boundaries are affected strongly. With increasing distance from the boundary the values for the loops approach those for the periodic boundary conditions. In the center of the lattice the average loops get stable.
The boundary effects for different lattice sizes in time direction are equal, the same amount of lattice points close to the boundaries are affected. Consequently, with increasing extent in time direction, the percentage of affected lattice points decreases. However, the usable central range is still reduced significantly. For $T = 16$, this range is approximately reduced by half. Therefore, a larger temporal extent is necessary for open boundary conditions to be advantageous. The results for lattice sizes $T = 16$ and $T = 32$ are shown in fig. 4.

The boundary effect for the first parallel plaquette is smaller than for the first perpendicular plaquette since in the calculation of the parallel, the distance from the boundary is slightly increased. Therefore, it is reasonable to set the position of the plaquettes as their center. So, parallel loops are shifted by 0.5 a. Through this definition of the position, the values lie on a continous curve approaching the center value. Obviously, this leads to one plaquette fewer for parallel than for perpendicular plaquettes. These differences are highlighted in fig. 4 and fig. 5 by using different colors for parallel and perpendicular plaquettes.

The values for the plaquettes from simulations with open boundary conditions approach the values obtained from periodic boundary conditions as they move further to the center of the lattice. This convergence corresponds to an exponential increase of the values for open boundary conditions toward the center of the lattice. That implies that those values can be calculated from the values for the periodic as follows:

$$\langle P_{\mu\nu} \rangle = \langle P_{\mu\nu,\text{ periodic}} \rangle \left(1 - e^{-\lambda t}\right). \tag{23}$$

Here λ is the rate at which the difference between open and periodic boundary conditions decays. It characterizes the range of boundary effects. Actually, boundary effects are slightly present in the center as well, which is why λ is the more important value for deciding which range in the center to use for further calculations.
If the logarithm of the normalized data is plotted according to $\ln\left(1 - \frac{\langle P_{\mu\nu}\rangle}{\langle P_{\mu\nu,\text{ periodic}}\rangle}\right)$, as a function of t, the values at the boundaries have a linear behavior. Near the center of the lattice, as the values for the open boundary conditions are similar to the periodic, the fraction approaches one, thus the logarithmic plot reduces to a linear function of time and λ can, in principle, be determined by a linear fit:

$$\begin{aligned}&\ln\left(1 - \left(1 - e^{-\lambda t}\right)\right)\\ &= \ln\ \left(e^{-\lambda t}\right)\\ &= -\lambda t.\end{aligned}$$

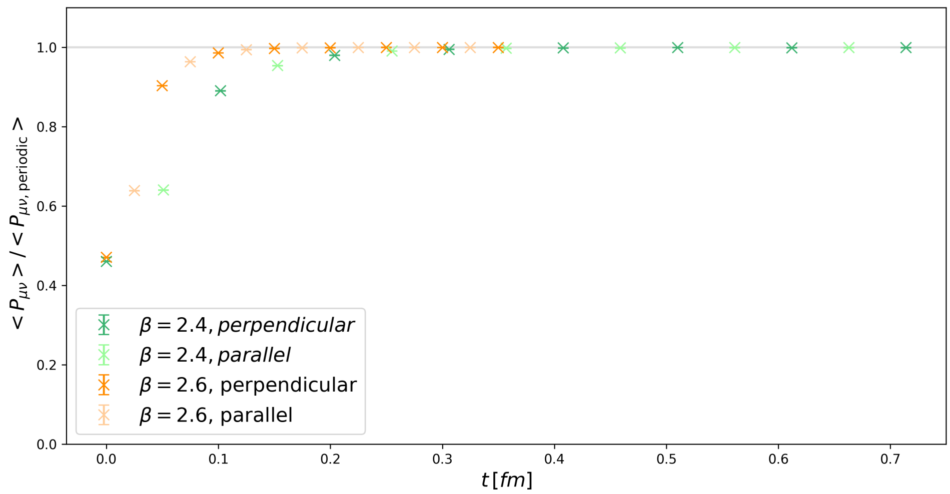

Figure 5: Boundary effects of plaquettes for $\beta = 2.4$ and $\beta = 2.6$, parallel and perpendicular.

The data shown in fig. 5 depend on the coupling constant β and thus on the lattice spacing a (table 1). It can be seen that for a smaller lattice spacing the same amount of lattice points is affected. So, the extension of the boundary effects in physical dimensions gets smaller when the lattice spacing decreases. In case of the same total extension in physical units, which leads to twice as many lattice points for a lattice spacing half as big, a larger distance is stable.

The average Wilson loop decreases with the loop extension getting bigger, independent of the boundary conditions. Thus the values for open boundary conditions approach the usual constants as the loops get closer to the center of the lattice. For larger lattice spacings a as well as for larger extensions of the loops, the affected range in physical units increases. The larger the loops the closer they get to the boundaries even if the starting point is close to the center of the lattice. This effect is shown in fig. 6 and fig. 7. As a consequence, the values for $\beta = 2.4$ increasingly remain at a certain distance from the values obtained with periodic boundary conditions as the loops size is raised. Also for perpendicular loops, the effects increase for wider loops, since more links contributing to one loop are affected. Obviously, the number of parallel loops that can be calculated without reaching beyond the lattice boundaries decreases.

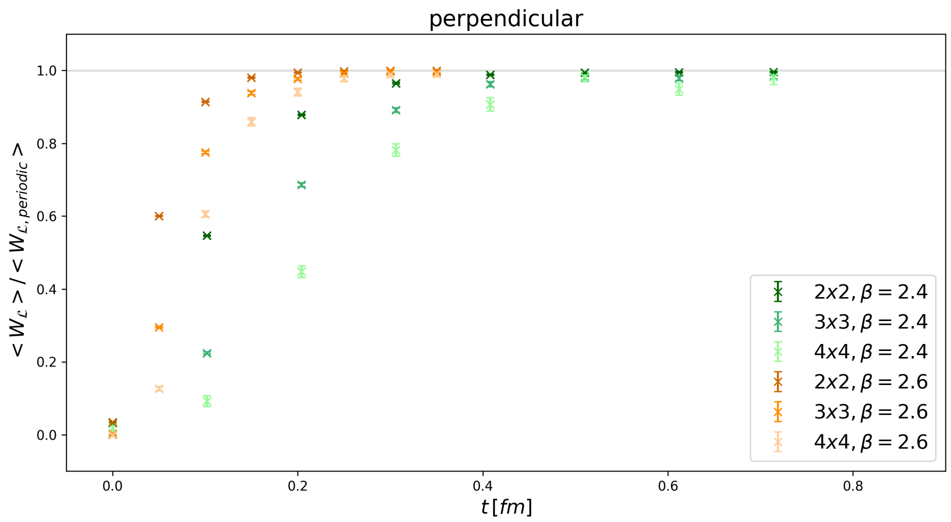

Figure 6: Boundary effects of perpendicular Wilson loops with different sizes for $\beta = 2.4$ and $\beta = 2.6$.

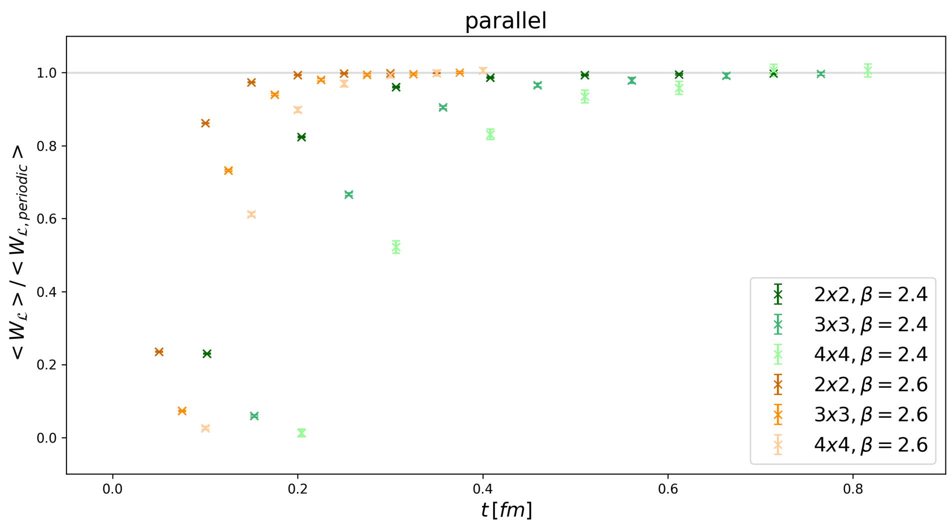

Figure 7: Boundary effects of parallel Wilson loops with different sizes for $\beta = 2.4$ and $\beta = 2.6$.

4.2 Topological charge

To decide whether using open boundary conditions improves the runtime efficiently and generates more unbiased results, the topological charge needs to be calculated. If the topological charge starts to freeze for periodic boundary conditions, open boundary conditions become efficient.
The topological charge was calculated for three different lattice spacings across 3000 configurations after 100 thermalization steps. The clover improvement was used and the UV-fluctuations were adjusted by APE-smearing with $\alpha = 0.3$ (see section C) until Q stabilizes for several smearing steps for most configurations. A total of ten smearing steps was found to be sufficient.

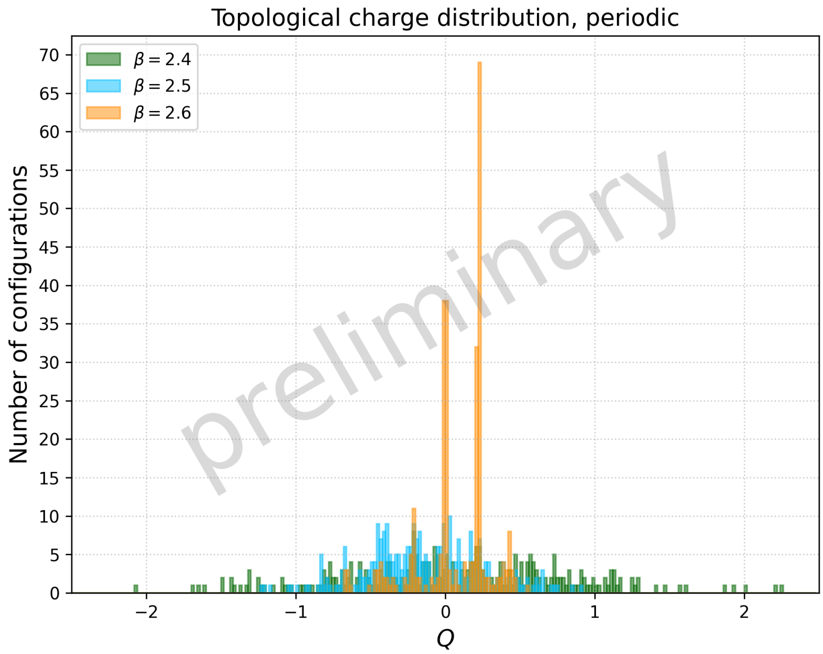

Figure 8: Histogram of the topological charge for different lattice spacings. The charge fluctuates less and peaks sharpen as the spacing decreases.

The histogram of the topological charge (fig. 8) illustrates the differences of the distributions for periodic boundary conditions as the lattice spacing decreases. It shows how often a given topological charge value was obtained across the different configurations.
It is important to note that the values do not yet align with integer values, a missing factor of 4 is assumed. Due to the limited time available for a Bachelors thesis, this could not be completed and solving this will be part of future work.

Nevertheless, we can observe that for $\beta = 2.4$ the distribution is wider and flatter, following the shape of a Gaussian function, as expected ([7]), with Q between -2.5 and 2.5. For this lattice spacing small peaks are already visible but not as high as for the smallest spacing. That is because the topological sectors exist but the energy barriers are small enough to allow a regular fluctuation between them. As the lattice spacing decreases, the distribution gets tighter and peaks become sharper. This effect becomes noticable for $\beta = 2.5$ and even more significant for $\beta = 2.6$. For $\beta = 2.6$ the peaks are much more isolated and higher which represents the effect of topological freezing. For small lattice spacings large topological charges cannot be reached. The peak to the right of zero is highest, probably due to the hot start. This is expected to diminish with more statistics when more configurations are considered.

When simulating with large lattice spacings, calculating the topological charge is not as efficient, because information might get lost. If the spacing is too coarse, it becomes unclear whether a feature is a knot or a curve.

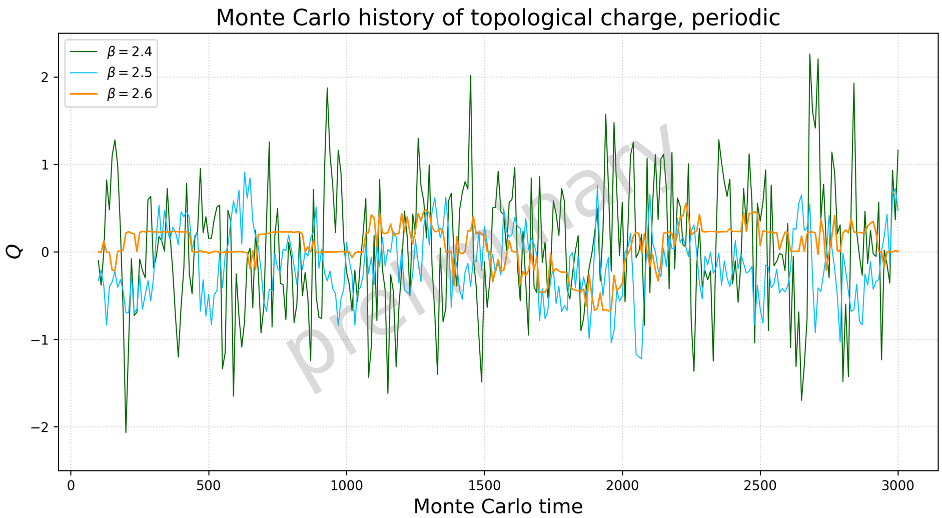

Figure 9: Monte Carlo history of the topological charge for different lattice spacings. As the spacing decreases, the charge fluctuates in a smaller range and remains constant for several steps, representing the effect of topological freezing.

The Monte Carlo history of the topological charge (fig. 9) for periodic boundary conditions shows the variation of the charge between consecutive configurations. For $\beta = 2.4$ the topological charge changes frequently and topological freezing is not a problem. As the spacing decreases, the range in which the charge fluctuates becomes smaller. For the smallest spacing $a = 0.05\,\text{fm}$ the values remain nearly constant for a few configurations before changing again. That means the autocorrelation time gets significantly longer and the effect of topological freezing appears. The data indicates that the autocorrelation time corresponds to several hundred Monte Carlo steps. Introducing open boundary conditions is expected to shorten the autocorrelation time by a significant factor. Thus the configurations transition faster between the different topological sectors and a proportionally shorter simulation time is sufficient to reach a set of configurations that is comparably representative. Consequently, the efficiency of the simulation is expected to increase, making open boundary conditions the preferable choice.

Here as well, the problem of a probably missing factor of four needs to be addressed in future work. Despite this, the results presented in this section indicate that the freezing of the topological charge becomes relevant for lattice spacings smaller than 0.05 fm. This suggests that open boundary conditions may be more effective for spacings below this value.

Topological susceptibility The values for the topological susceptibility χ are measures for the width of the Gaussian distribution (fig. 8) and the fluctuations of the topological charge. The values of χ were determined and are presented in table 2.

β	$\chi^{1/4}$ [MeV]
2.4	101
2.5	107
2.6	122

Table 2: Topological susceptibility for periodic boundary conditions dependent on the lattice spacing (preliminary).

The values are approximately half as large as the expected value [8]. An additional factor of four for the topological charge would lead to a factor of two for the susceptibility, so the determined values would better align with the expected. Despite this, our results are in good agreement with those of reference [8].

5 Conclusion

In this thesis, boundary effects have been studied in the context of open boundary conditions in time direction within $SU(2)$ Yang-Mills theory.
The boundary effects exhibit symmetry and the average values of loops approach those of periodic boundary conditions, decaying exponentially and becoming stable in the center of the lattice.
As the lattice size is increased in lattice units, the absolute distance over which boundary effects extend remains constant in lattice units. Consequently, the percentage of affected lattice points decreases. The boundary effects have approximately the same distance in lattice units for different lattice spacings a, which corresponds to a shorter physical distance when using a smaller lattice spacing.
For larger Wilson loops, the range in which the values remain stable shrinks as the loop size increases. The boundary effects become stronger and more extensive as the loops reach closer to the boundaries. This is the case also for perpendicular loops, since more links contributing to a single loop are influenced by the boundaries.

This needs to be considered carefully e.g. when calculating the static quark-antiquark potential, which includes large Wilson loops. The range of the usable, stable region in the center of the lattice needs to be selected cautiously. Increasing the number of lattice points in the open direction helps to widen the stable range. Since the potential includes loops in time direction, it is preferable to implement open boundary conditions in a spatial direction analogously instead.

To decide whether open boundary conditions lead to an increased efficiency, the topological charge was calculated for periodic boundary conditions. As the lattice spacing decreases the topological charge distribution narrows and peaks sharpen due to the longer autocorrelation time. For spacings $a < 0.05\,\mathrm{fm}$ topological freezing becomes relevant. Open boundary conditions are expected to be the better choice for spacings below this value, though the lattice size needs to be chosen larger.

5.1 Outlook

Future work includes a detailed investigation of the topological charge calculation, as a discrepancy by a factor of four compared to the expected values has been observed. The APE-smearing and the calculation of the topological charge need to be adjusted for open boundary conditions. The fluctuation of the topological charge for both boundary conditions can be compared as well as the movement of the topological charge on the lattice. Extending the analysis to SU(3) is important for realistic lattice QCD computations.

To achieve improved results for the topological charge, the Symanzik improvement, which uses 2x1 rectangular loops, or the 3-loops improved topological charge operator can be used. To get integer values, errors below $\mathcal{O}(a^6)$ need to be suppressed. For further detail see [6].

Alternatively to open boundary conditions, a non-orientable manifold can be used. This is constructed by replacing the periodic boundary condition in time direction by a "P-periodic" boundary condition, which means, the fields are parity transformed across the boundary. This reduces the autocorrelation time drastically compared to periodic boundary conditions, while translational invariance is preserved up to exponentially small corrections. In this case, the topological charge also becomes continuous and fluctuates faster compared to periodic boundary conditions. One does not have boundary effects in this case. For further information, see reference [4].
Another interesting topic related to this thesis is using different coupling constants in different directions of the lattice. This is analyzed in the Bachelor thesis of Emre Akinc and as well aims to allow simulations with smaller lattice spacings. Both approaches can be combined.

Appendix

A Thermalization

The thermalization of plaquettes for periodic and open boundary conditions is compared in fig. 10. They thermalize at the same speed, as well as the Wilson loop averages (fig. 11). For periodic boundary conditions all values at different positions approach the same value while for open boundary conditions the values decrease when their position is closer to the boundaries.

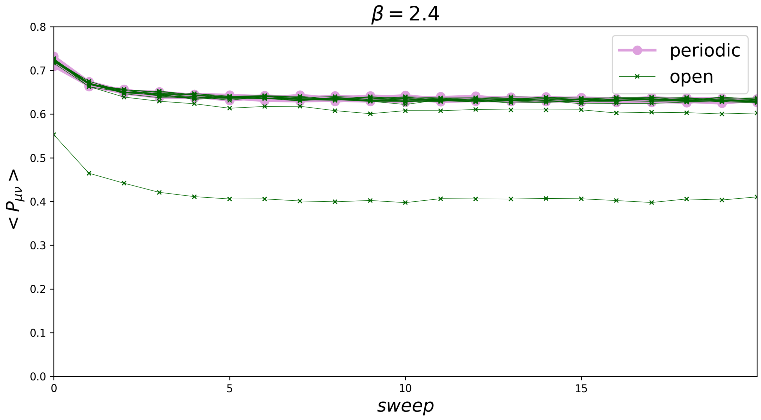

Figure 10: Thermalisation of the average of perpendicular plaquettes compared for periodic and open boundary conditions, for $\beta = 2.4$ and $T = 16$. The different green curves represent varying distances from the boundaries. The values calculated near the center overlap with those obtained with periodic boundary conditions, while values closer to the boundaries increasingly thermalize at lower values.

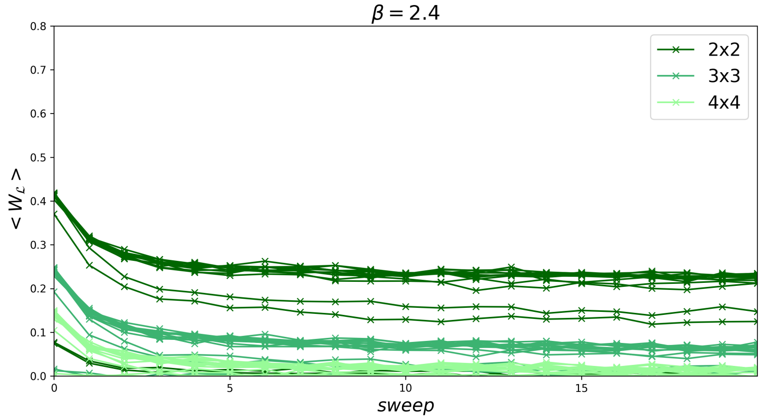

Figure 11: Thermalisation of the average of perpendicular Wilson loops with open boundary conditions, for $\beta = 2.4$ and $T = 16$. The different green curves represent varying distances from the boundaries for each loop size. The closer to the boundary, the lower the values they thermalize at.

B Binning and Jackknife method

Due to the autocorrelation between consecutive configurations, binning and the jackknife method are necessary to determine errors. The values, omitting the configurations in the thermalization range, are binned. This reduces autocorrelation, leading to a more reliable error estimation.
In the Jackknife method, particularly, reduced samples are used. Binning is applied and calculations are performed for a value in comparison to the bin average. The standard deviation σ_θ can be calculated with the averages of all bins and of the inverse bins $\tilde{X}_i$ [10]:

$$\tilde{X}_i = \frac{1}{N-1}\left(\sum_{m=1}^{N} x_m - x_i\right), \tag{24}$$

$$\sigma_\theta = \sqrt{\frac{N-1}{N}\sum_{i=1}^{N}\left(\theta_i - \hat{\theta}\right)^2}. \tag{25}$$

Here, N is the number of the bins, θ_i are the means of the inverse bins and $\hat{\theta}$ the mean of all bins. This method is used to deal with autocorrelation and for the potential's error, since error propagation must be considered. Also, as the values for the Wilson loops approach zero, the error ranges may extend into the negative region. This is problematic because taking the logarithm of negative values is undefined.
In this thesis, all errors are obtained via the jackknife method.

The errors for perpendicular plaquettes are calculated for different bin sizes at each position along the time direction, as shown in fig. 12. For a certain range of bin sizes, the errors are nearly constant. For the results shown in section 4.1, a bin size of 35 was used.

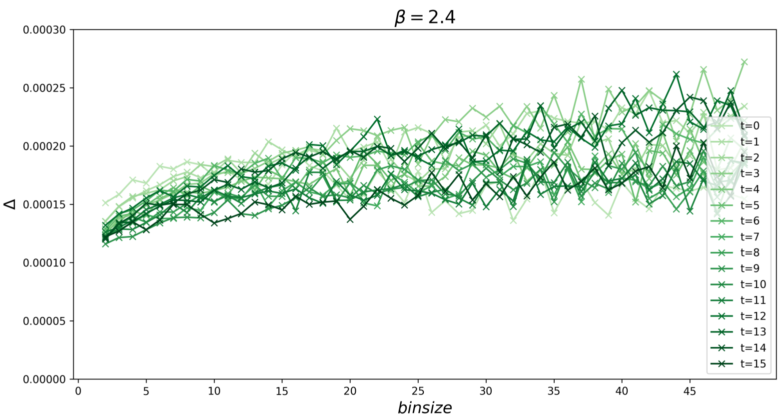

Figure 12: Errors Δ of perpendicular plaquettes for different bin sizes, obtained from the jackknife method, for $\beta = 2.4$ and $T = 16$.

C APE-smearing

Correlation functions and long distance behavior might be affected by short distance fluctuations of the gauge field. To avoid this, the gauge field is smeared by replacing link variables by local averages over short paths with fixed endpoints which does not affect the long distance correlation signals in the continuum limit.
When using the APE-smearing, the original gauge link is replaced by the average of itself and the six staples connecting its endpoints: [5]

$$V_\mu(n) = (1-\alpha)U_\mu + \frac{\alpha}{6}\sum_{\nu\neq\mu} C_{\mu\nu}(n), \tag{26}$$

$$C_{\mu\nu}(n) = U_\nu(n)U_\mu(n+\hat{\nu})U_\nu(n+\hat{\mu})^\dagger + U_\nu(n-\hat{\nu})^\dagger U_\mu(n-\hat{\nu})U_\nu(n-\hat{\nu}+\hat{\mu}). \tag{27}$$

When smearing to calculate the topological charge, it is important to smear out only the UV-fluctuations. If the APE-smearing is applied too frequently, also instantons can be erased.
In the calculations $\alpha = 0.3$ was used.

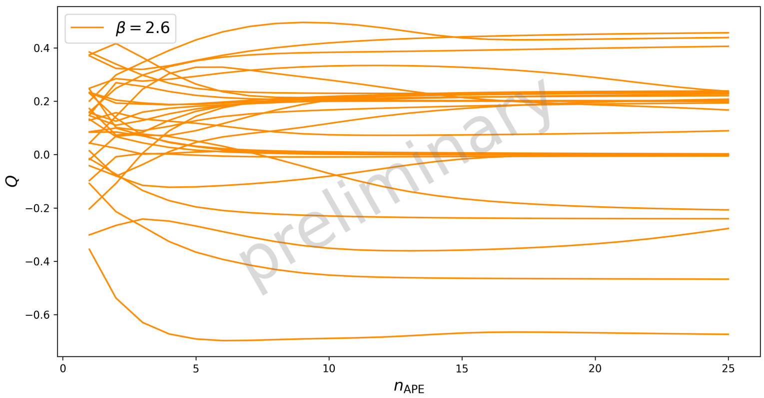

Figure 13: APE-smearing history of the topological charge for periodic boundary conditions. Values for the topological charge calculated for different configurations with $\beta = 2.6$ convere to plateaus and become stable during the smearing process.

The change of the topological charge values for different configurations, depending on the number of smearing steps, is shown in fig. 13. The values of the topological charge converge to plateaus and become stable. With further smearing steps, they are expected to converge even more, until the smearing erases instantons, which would lead to a change in the values. This erase of instantons does not occur for 25 smearing steps and thus does not affect our calculations, which are performed with only ten steps.

D Gauge invariance

To verify the correctness of the code and ensure that the observables are gauge-invariant as required, a random gauge transformation $g(x) \in SU(2)$ is applied to the gauge field:

$$U_\mu(x) \to g(x)U_\mu(x)g^\dagger(x + e_\mu). \tag{28}$$

Observables need to have the same value before and after the gauge transformation. This is implemented by generating a random gauge transformation $g(x)$, that does not have a direction. A random value for every link in one direction is chosen, while all links in the other three directions are set to $\mathbf{1}$. The observables, such as plaquettes, Wilson loops and the topological charge, are first computed on the initial gauge field. After applying the transformation the observables are calculated again. The results must be equal to prove gauge invariance. In particular, this test shows if all used loops are closed. If incorrect indices are used, the loops will have a hole, leading to a violation of the gauge invariance.

References

[1] Wagner, M., Diehl, S., Kuske, T. & Weber, J. An introduction to lattice hadron spectroscopy for students without quantum field theoretical background. arXiv: 1310.1760 [hep-lat] (2013).

[2] Philipsen, O. *Quantenfeldtheorie und das Standardmodell der Teilchenphysik: Eine Einführung* 10.1007/978-3-662-57820-9 (Springer, 2018).

[3] Lüscher, M. & Schaefer, S. Lattice QCD without topology barriers. *JHEP* **07,** 036. arXiv: 1105.4749 [hep-lat] (2011).

[4] Mages, S. *et al.* Lattice QCD on nonorientable manifolds. *Phys. Rev. D* **95,** 094512. arXiv: 1512.06804 [hep-lat] (2017).

[5] Gattringer, C. & Lang, C. B. *Quantum Chromodynamics on the Lattice: An Introductory Presentation* Lecture Notes in Physics, **788** 10.1007/978-3-642-01850-3 (Springer, 2010).

[6] Dromard, A. Extracting physics from fixed topology simulations. Dissertation, Goethe Universität Frankfurt am Main (2016).

[7] Schlosser, C. & Wagner, M. Hybrid static potentials in SU(3) lattice gauge theory at small quark-antiquark separations. *Phys. Rev. D* **105,** 054503. arXiv: 2111.00741 [hep-lat] (2022).

[8] Forcrand, P. d., Perez, M. G. & Stamatescu, I.-O. Topology of the SU(2) vacuum: a lattice study using improved cooling. *Nucl.Phys.* **B499,** 409–449. arXiv: 9701012v2 [hep-lat] (1997).

[9] Philipsen, O. & Wagner, M. On the definition and interpretation of a static quark antiquark potential in the colour-adjoint channel. *Phys. Rev. D* **89,** 014509. arXiv: 1305.5957 [hep-lat] (2014).

[10] Riehl, C. Hybrid static potentials at small lattice spacings and possible glueball decay. Master's thesis, Goethe Universität Frankfurt am Main (2019).

List of Figures

List of Tables